atmosphere

MDPI

Article

Impact of Lens Angle and Nozzle Geometry on Aerodynamic Focusing: A Numerical Study

Apolo Vannavong [1], Harrison Griffin [1,†], Xiaoliang Wang [2,*] and Mustafa Hadj-Nacer [1,*]

[1] Mechanical Engineering Department, University of Nevada, Reno, NV 89557, USA
[2] Division of Atmospheric Sciences, Desert Research Institute, Reno, NV 89512, USA
* Correspondence: xiaoliang.wang@dri.edu (X.W.); mhadjnacer@unr.edu (M.H.-N.)
† Current address: Raytheon, 9000 S Rita Rd, Tucson, AZ 85747, USA.

Abstract

Straight-edge thin plate orifices (90° half-angle) are used as the focusing elements in most aerodynamic lenses. They are simple to fabricate and have fewer boundary-layer effects as compared to other geometries, such as capillaries and converging and diverging orifices. This study presents the first systematic evaluation of lens focusing performance across a wide range of half-angles. Computational fluid dynamics (CFD) simulations and Lagrangian particle tracking were used to investigate aerodynamic focusing of converging, straight-edge, and diverging orifices with half-angles ranging from 30° to 150° at two Reynolds numbers (50 and 100) and three Mach numbers (0.03, 0.1, and 0.3). The results show that the optimal Stokes number for near-axis particles has small differences between the straight-edge orifice and the converging or diverging orifices, indicating small changes in focusing behavior for different orifice geometries. This study further optimized exit nozzle dimensions to enhance focusing. Several nozzle radial aspect ratios and nozzle constriction lengths were simulated in a two-dimensional axisymmetric domain. The optimal geometry was identified for generating the least divergent particle beams and maintaining the highest transmission efficiencies for 10 nm–10 μm particles. Identifying such a nozzle geometry is critical for future designs of more efficient aerodynamic focusing lenses.

Keywords: aerodynamic lenses; aerodynamic focusing; orifice; capillary; nozzle; CFD

check for updates

Academic Editors: Avelino Eduardo Saez and Alan Robins

Received: 19 June 2025
Revised: 26 August 2025
Accepted: 29 August 2025
Published: 3 September 2025

Citation: Vannavong, A.; Griffin, H.; Wang, X.; Hadj-Nacer, M. Impact of Lens Angle and Nozzle Geometry on Aerodynamic Focusing: A Numerical Study. *Atmosphere* **2025**, *16*, 1049. https://doi.org/10.3390/atmos16091049

Copyright: © 2025 by the authors. Licensee MDPI, Basel, Switzerland. This article is an open access article distributed under the terms and conditions of the Creative Commons Attribution (CC BY) license (https://creativecommons.org/licenses/by/4.0/).

1. Introduction

Atmospheric aerosols play a key role in air quality, climate, and human health. Aerosol mass spectrometers (AMS) are widely used to measure atmospheric aerosols' chemical and physical properties. A key component of an AMS system is the aerodynamic focusing lens inlet (AFL), which uses a series of focusing orifices (lenses) to generate a concentrated, low-diverging beam of particles for more efficient sizing, collection, and/or ionization in the AMS [1–4].

A number of lens geometries, such as straight-edge thin plate orifices, capillaries, converging orifices, and converging–diverging orifices, have been used for generating molecular or aerosol beams [5–8]. The most common lenses used in AFLs are straight-edge thin plate orifices, favored for their strong focusing performance, minimal boundary effects, and ease of fabrication and integration into an AFL [9–14].

Fernández de la Mora et al. [15,16] examined the optimal Stokes number (St_o) for which particles are perfectly focused along the axis as a function of half-angle, α, for several

lens geometries, i.e., capillary ($\alpha = 0°$), converging orifice ($0° < \alpha < 90°$), straight-edge thin plate orifice ($\alpha = 90°$), and diverging orifice ($90° < \alpha < 180°$) (see Figure 1). They found that St_o decreased with increasing α, indicating that diverging orifices might better focus smaller particles. To the best of our knowledge, no numerical or experimental studies have examined particle focusing using a diverging orifice, other than those by Fernández de la Mora et al. [15,16], who did not show detailed flow fields or explain why diverging orifices would have a smaller St_o. Middha et al. [17] simulated particle focusing in a sonic jet through a nozzle consisting of a cap and a cone, with α ranging from 90° to 130°. They found that a diverging sonic nozzle had a smaller St_o than thin plate orifices. Because the low inertia and high diffusivity are key barriers to effectively focusing nanoparticles [18–20], lenses with smaller St_o enable smaller particles to be optimally focused. They also allow the lenses to operate at higher pressures to reduce diffusion broadening. Therefore, diverging orifices can potentially improve the focusing of particles with aerodynamic diameters of <30 nm in subsonic, low-Reynolds number (Re) conditions [19]. However, in a subsonic (Mach number, Ma < 0.3) and low-Re (<200) flow, it is possible that the flow near the edges where the orifice contacts the wall stagnates and traps particles; the viscous boundary layer around the walls might make the flow velocity non-uniform. This demonstrates the significance of further investigating the flow field and particle trajectories through diverging orifices.

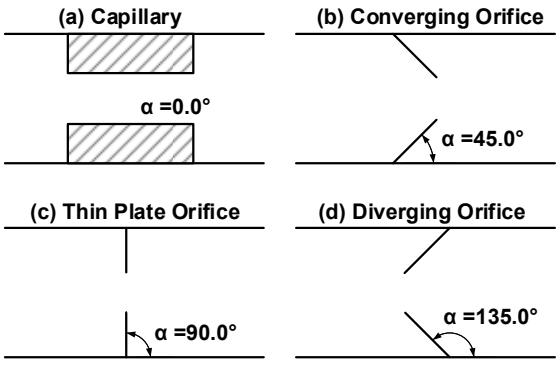

Figure 1. Examples of orifices with different values of α.

The AFL's accelerating exit nozzle is also a critical part, as it controls the AFL's internal pressure and accelerates the particles into the vacuum chamber. The nozzle often has an aperture that is smaller in diameter than the lenses; thus, it may focus smaller particles and defocus larger particles. The higher Re at the nozzle may generate turbulence and disperse the particle beam. Liu et al. [10] examined the particle trajectories of a step nozzle consisting of a cylindrical constriction followed by a thin plate orifice. They found a specific combination of step length, step diameter, orifice diameter, and flow rate that generated the least particle divergence. Zhang et al. [21,22] confirmed that this design performed the best among several different geometries. They also found that a smooth converging nozzle used in the AMS had higher divergence than Liu's design for particles <50 nm [23]. Many AFL designs emphasize the focusing by lenses, with little attention paid to potential focusing or defocusing at the exit nozzle. A proper design of a step nozzle would refocus larger particles, which tend to become defocused in the last lenses and the exit nozzle. Furthermore, a short capillary instead of a thin plate orifice might reduce the beam spread in the vacuum, as capillaries offer smaller divergence angles for wider particle size ranges [3].

To address these knowledge gaps, single aerodynamic focusing lenses with varying values of α are numerically modeled using computational fluid dynamics (CFD) and Lagrangian particle tracking to investigate whether converging or diverging lenses improve particle focusing. Additionally, the behavior of particles traveling through step accelerating

nozzles with varying dimensions of interest is numerically studied to find an optimal design that yields the lowest beam divergence and highest transmission efficiency for 10 nm–10 μm particles.

2. Model Descriptions and Methods

2.1. Converging and Diverging Lens Model

Flow through a single lens with different values of α was simulated with 2D axisymmetric models using the finite volume method (FVM) in ANSYS FLUENT (R2 2022) [24]. As shown in Figure 2, this model consists of two spacer regions separated by a 0.3 mm thick lens with an orifice (lens) radius of 1 mm. The spacers have a length of 60 mm and a radius of 5 mm. Nine values of α (30°, 45°, 60°, 75°, 90°, 105°, 120°, 135°, and 150°) were simulated for two of Re (50 and 100) and three of Ma (0.03, 0.1, and 0.3).

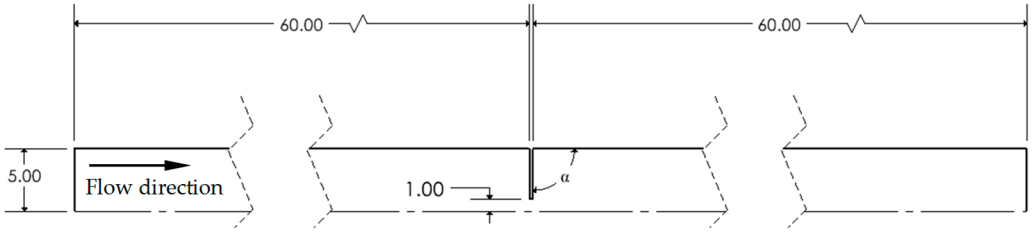

Figure 2. Two-dimensional (2D) axisymmetric model used for the divergent lens study. Units in millimeters.

The boundary conditions consist of a fixed mass flow rate at the inlet and a fixed pressure at the outlet. Wall surface roughness is neglected, assuming perfectly smooth walls. More details on the boundary conditions are provided in Supplementary Materials S1. Given the low Re considered for the simulations, a steady-state laminar viscous flow model was employed. The effect of gravity was assumed to be negligible. The air density was calculated using the ideal gas law, and Sutherland's model was used for air viscosity [25]. Particles were modeled as perfect spheres of liquid water droplets with a constant density of $\rho_p = 998.1\ \mathrm{kg/m^3}$. A user-defined function was used to calculate the drag force based on local flow conditions [9,19]. Particles' Brownian motion was not accounted for [11]. Particles were considered to be trapped when the distance between the particle center and the wall was smaller than the particle radius.

A mesh sensitivity study was conducted with four meshes with increasing rectangular cell counts, as detailed in Supplementary Materials S2, based on [26]. The mesh consisting of ~50,000 cells was deemed sufficient, as the results were independent from further refinement.

Two criteria were used to evaluate lens performance: the particle contraction factor, η_c; and $\mathrm{St_o}$. η_c, defined as the ratio of the particle's radial position (r_{p2}) downstream of the lens to its initial radial position (r_{p1}) upstream of the lens, indicating how the lens alters the trajectory of a particle. $\eta_c < 1$ indicates focusing, while $\eta_c > 1$ indicates defocusing. Particles with $\eta_c = 0$ are perfectly focused on the axis, and their corresponding particle Stokes number (St) is defined as $\mathrm{St_o}$. St is the ratio of a particle's relaxation time, τ, multiplied by the average flow velocity (u) over the lens diameter (d_f) [9,11]:

$$\mathrm{St} = \frac{\tau u}{d_f} = \frac{2\rho_p \dot{m} d_p^2 C_c}{9\pi\rho_1 \mu d_f^3}, \quad (1)$$

where ρ_p and ρ_1 are the densities of particles and air upstream of the lens, respectively, $\dot{m}$ is the mass flow rate of air, d_p is the particle diameter, μ is the air viscosity, C_c is the

Cunningham correction factor with $C_c = 1 + Kn_p(1.257 + 0.4e^{\frac{-1.1}{Kn_p}})$, Kn_p is the particle Knudsen number with $Kn_p = 2\lambda_1/d_p$, and λ_1 is the mean free path of the gas upstream of the lens.

Due to boundary-layer effects, particle trajectories depend on their initial radial locations. Five radial locations (Δ = 0.1, 0.3, 0.5, 0.7, and 0.9), defined as the ratio of the particle's initial radial location (r_{p1}) to the radius of the spacer (r_s) upstream of the lens, were investigated. A total of 283 particles, ranging in diameters from 1 nm to 10 µm, were injected at each radial location to evaluate η_c and St_o.

2.2. Nozzle Model

To evaluate the performance of a step nozzle in focusing particles, a 2D axisymmetric model of an exit nozzle with an expansion chamber was generated and simulated using the FVM in ANSYS FLUENT (R2 2022) [24]. Figure 3 shows a schematic of this model, which consists of a spacer with a length of 60 mm and a radius of 5 mm, a capillary step with a length of L_t and a step-to-spacer radius ratio of R_t, an accelerating nozzle with a thickness of L_n and radius of 1.5 mm, and a vacuum expansion chamber. Air enters the inlet of the spacer at a fixed mass flow rate of 3×10^{-6} kg/s and contracts and accelerates through the step and nozzle into a vacuum expansion chamber. A fixed pressure of 1 Pa was applied on the outlet boundaries of the vacuum expansion chamber to simulate the particle-sizing region in an AMS. The flow was assumed to be steady-state in the continuum regime, so gas rarefaction effects were not considered. The same air and particle properties used for the converging/diverging lens simulations (see Section 2.1) were applied in this model. A mesh sensitivity study (in Supplementary Materials S2) was also conducted for this model and showed that a mesh of approximately 7 million rectangular cells was sufficient for the independence of the results from further mesh refinements.

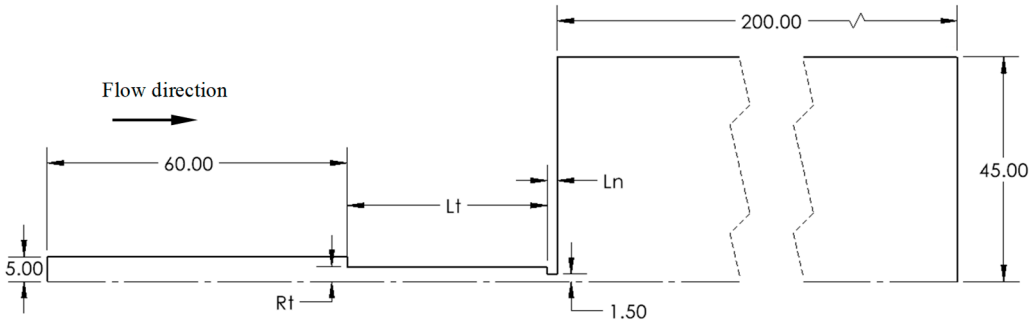

Figure 3. Two-dimensional (2D) axisymmetric model used for nozzle simulations. Units in millimeters.

Figure 3 shows the three variable dimensions of interest of the step nozzle design: thickness of the nozzle (L_n), length of step (L_t), and ratio of the step radius to the spacer radius (R_t). Six L_n (i.e., 0.254, 0.5, 1, 2, 5, and 10 mm), nine L_t (i.e., 10, 20, 30, 40, 50, 60, 70, 80, and 90 mm), and five R_t (i.e., 0.4, 0.5, 0.6, 0.7, and 0.8) values were investigated. All of the other dimensions, including the spacer and vacuum expansion chamber diameters and lengths, remained fixed. To systematically evaluate the particle focusing performance, L_n was first varied with a fixed value of L_t = 10 mm and R_t = 0.6. Once the optimal L_n value was determined, it was fixed, and then L_t was varied with the same fixed value of R_t = 0.6. In a similar manner, once the optimal L_t value was identified, it was fixed as well, and R_t was finally varied. This process ensured that the most optimal combination of all three dimensions was determined.

Two criteria were used to evaluate the AFL nozzle performance: particle divergence angle in the expansion chamber, and transmission efficiency. The particle divergence angle

(θ) is defined as the terminal departure angle of a particle exiting the nozzle outlet. It is calculated as the inverse tangent of the particle's radial velocity ($u_{y,p}$) divided by its axial velocity ($u_{x,p}$) component:

$$\theta = arctan\left(\frac{u_{y,p}}{u_{x,p}}\right) \quad (2)$$

where θ = 0 indicates that the particle travels parallel to the nozzle's axis. The closer the divergence angle is to zero, the better the performance of the nozzle. To evaluate θ, 500 unique particles, ranging from 10 nm to 10 µm, were injected at a single near-axis radial location, Δ = 0.1. Particle velocities were measured at 30 mm downstream of the nozzle exit, after the particles had reached their terminal trajectory in the vacuum expansion region.

Transmission efficiency, η_t, is defined as the ratio of the number of particles reaching the outlet of the AFL nozzle (N_2) to that injected at the inlet (N_T):

$$\eta_t = \frac{N_2}{N_T} \quad (3)$$

Perfect transmission efficiency is achieved when all injected particles reach the nozzle outlet, i.e., η_t = 1. A transmission efficiency > 0.5 is typically considered sufficient for the AFL system [11]. To calculate η_t, 300,000 monodisperse particles were injected at 15 mm downstream of the inlet across the entire radius of the spacer. Particles were distributed across the radius of the spacer according to the following function:

$$r_i = d_s\left(1 - \frac{1 - \sqrt{i - 0.5}}{N_T}\right)^{0.5} \quad (4)$$

where r_i is the particle radial seeding location for particle i, and d_s is the spacer diameter. This function ensures a uniform particle mass flux across the inlet. A total of 300 particle sizes, in the diameter range 10 nm to 10 µm, were simulated, with each size injected from 1000 radial locations (r_i = 1000).

3. Results

3.1. Effects of Lens Half-Angle

Figure 4a shows η_c as a function of St for Re = 50 and Ma = 0.1 with an injection location Δ = 0.1, comparing three values of α (30°, 90°, and 150°). For clarity, results with lens half-angles of 45, 60, 75, 105, 120, and 135 are omitted. Similar to the results obtained from previous works [9,21], η_c decreased from nearly 1 at small St (≈0.01) with minimal focusing, to zero at intermediate St (0.6–1.0) with strong focusing, and to negative values at larger St, indicating axis crossing. The three curves in Figure 4a are nearly identical, showing that the effect of α is negligible for particles injected near the axis, especially at St < 1.

Figure 4b shows the same results as Figure 4a, but for an injection location of 0.9. At this injection location, the particles travel more slowly than those injected near the axis, because of the boundary-layer effect. Similar to Δ = 0.1, minimal focusing is achieved at small St (≈0.01). However, for larger values of St, the curve of η_c for an α = 30° deviates significantly from that of the other angles. The convergent lens (α = 30°) focuses large particles better because it gradually converges particles toward the axis. For the straight-edge (90°) and divergent (150°) lenses, the particles follow a more abrupt converging flow, resulting in a flipped S trajectory to pass through the orifice, which causes large particles to deviate more from the axis.

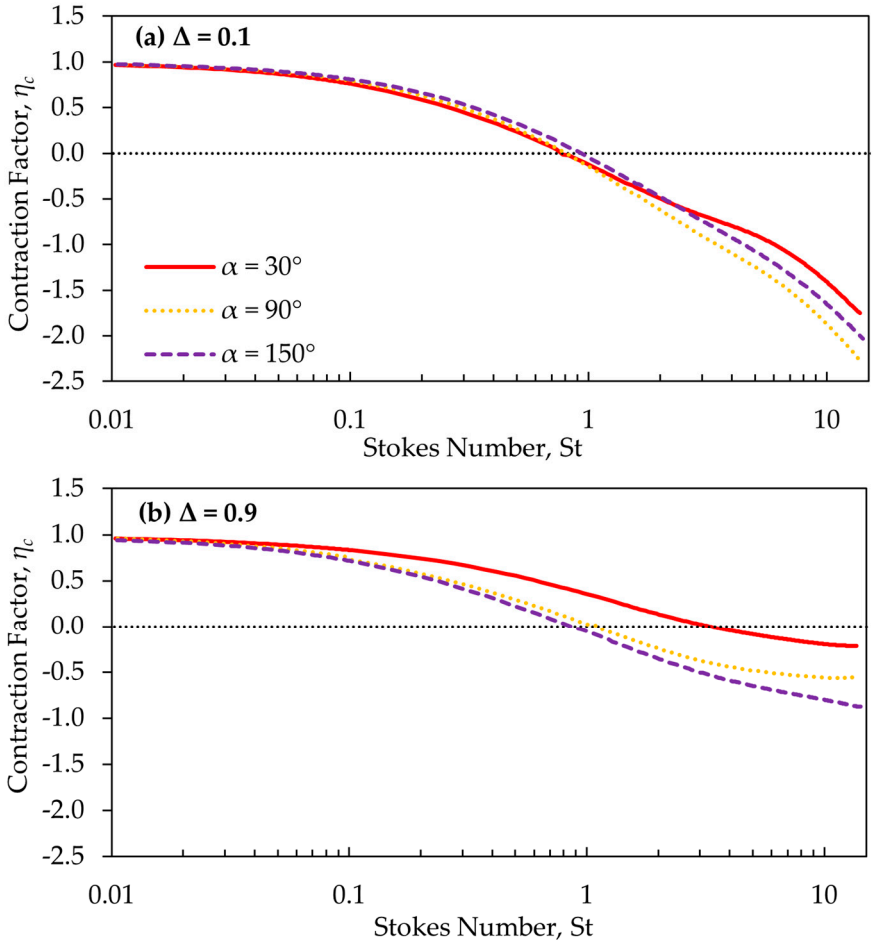

Figure 4. η_c as a function of St at Re = 50 and Ma = 0.1, for three different values of α (30°, 90°, 150°) and for two injection locations (**a**) Δ = 0.1 and (**b**) Δ = 0.9.

Figure 5 shows St_o as a function of α for near-axis injections (Δ = 0.1) at Re = 50 and different Ma (the data for Δ = 0.1 at Re = 100 is provided in Figure S4). For Re = 50, St_o varied within a narrow range, from 0.6 to 1.05. Converging lenses from 45° to 75° had the smallest St_o. In the free molecular regime, St is proportional to the vacuum aerodynamic diameter. Changing from a straight-edge lens (α = 90°) to a 45° converging lens would reduce the optimally focused particle size from 30 to 25 nm under the same flow conditions, a marginal impact. Interestingly, the diverging lenses (α > 90°) do not reduce St_o when particles are injected close to the axis, contrary to the prediction by Fernández de la Mora et al. [15,16]. Therefore, diverging half-angle lens designs do not show a pronounced improvement in focusing particles <30 nm. This contradiction is mainly due to viscous flow forces being taken into consideration in our model. However, particles injected far from the axis (close to the spacer wall, Δ = 0.9), regardless of Re, exhibit a decrease in St_o with increasing α, as shown in Figures S5 and S6.

Figure 6 illustrates particle trajectories through a 90° lens and a divergent 150° lens. The 150° lens has a larger stagnation region upstream of the lens. Particles only penetrate slightly into the stagnation layer and make a flipped S-shaped turn. However, the particles do not enter the stagnation layer deep enough to make two turns, making the difference with a 90° lens small. Since α does not have a significant effect on η_c or St_o, especially for particles near the axis, the 90° lenses are deemed to be a better choice due to their simplicity.

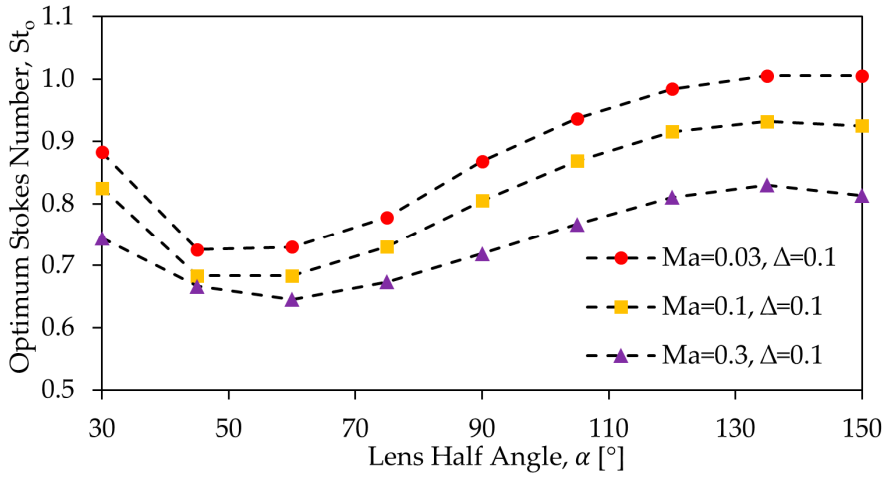

Figure 5. St_o as a function of α for three Ma values (0.03, 0.1, and 0.3) for near-axis particles (Δ = 0.1) at Re = 50. See Supplementary Materials S3 for Re = 100 with Δ = 0.1 in Figure S4, and for Re = 50 and 100 with Δ = 0.9 in Figures S5 and S6, respectively.

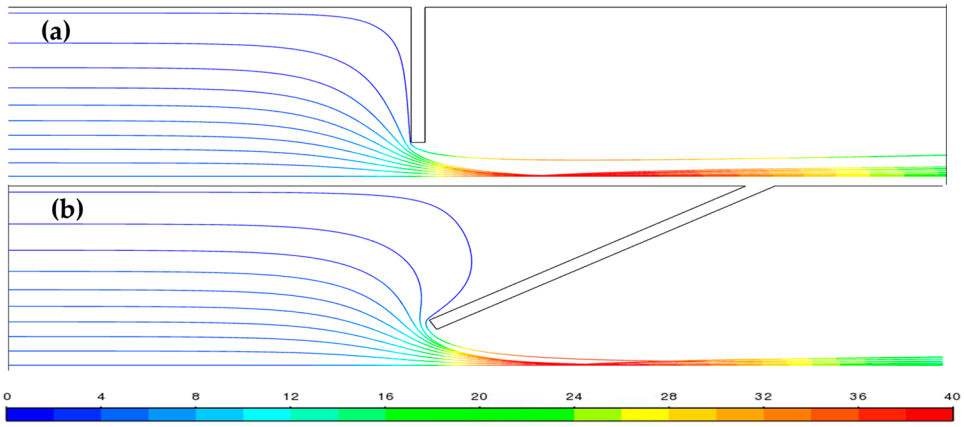

Figure 6. Trajectories of 900 nm particles (St = 1) through (**a**) a straight-edge lens with α = 90° and (**b**) a diverging lens with α = 150° at Re = 50 and Ma = 0.1. The lines are colored by particle velocities [m/s].

3.2. Effect of Exit Nozzle Geometry

3.2.1. Nozzle Thickness

Figure 7a,b show the particle divergence angle, θ, and the transmission efficiency, η_t, respectively, as a function of St for various values of L_n with a fixed L_t = 10 mm and R_t = 0.6. In these and subsequent figures (Figures 8 and 9), St is calculated using d_s = 10 mm as the characteristic dimension and the flow conditions at 30 mm downstream of the inlet, where the flow is fully developed.

Figure 7a shows that the dependency of the divergence angles on St is similar for all L_n values, except for short capillaries of L_n = 5 and 10 mm. Small particles (St < ~0.007), regardless of L_n, have the highest divergence angle from the center axis. This is because these particles have very small mass and inertia, making them closely follow the gas flow to expand radially outward at the nozzle exit into the vacuum chamber. The divergence angle decreases rapidly as St increases. Depending on L_n, the particles in the St range of ~0.01–0.03 achieve a divergence angle of zero. As St further increases, the divergence angle becomes negative, and its absolute value slightly increases, then decreases at high St values. A negative divergence angle means that the particles are converging toward the axis, ultimately diverging far from it in the opposite direction. Particles with a large St have a large inertia and are not significantly affected by the drag forces experienced at the nozzle

exit. The high inertia causes these particles to move across the axis, resulting in negative divergence angles.

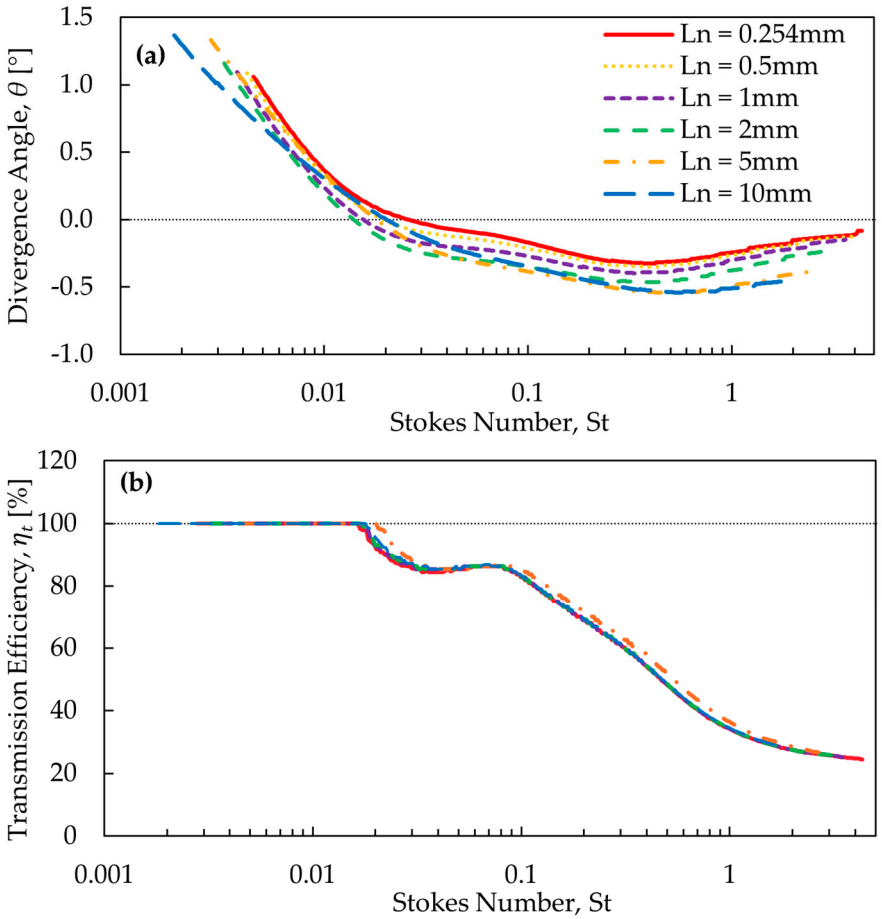

Figure 7. Results from the nozzle simulations of (**a**) θ and (**b**) η_t for various values of L_n as a function of St.

Figure 7a also shows that, for St $\gtrsim$ 0.02, the thinnest nozzle (L_n = 0.254 mm) maintains the smallest absolute divergence angle. This feature will reduce defocusing and even enable focusing of larger particles by the nozzle. The short capillaries generate lower divergence angles for smaller particles (St $\lesssim$ 0.02) but do not reduce the beam spread over a wide size range. Therefore, thin plate nozzles are recommended as the AFL exit. The thickness of 0.254 mm (i.e., 0.1 inch) is recommended for sufficient mechanical strength.

Figure 7b shows that the η_t curves follow a similar trend, regardless of L_n. As expected, small particles (St $\lesssim$ 0.017) maintain a 100% η_t for all L_n values. At St $\approx$ 0.018, the η_t drops below 100% to about 85% at St $\approx$ 0.04, remains nearly constant (slightly increases) until St $\approx$ 0.1, and then steadily decreases afterward. The near-constant η_t values at St $\approx$ 0.04–0.1 are directly related to the effect of the step radius, R_t, which will be discussed in Section 3.2.3. An η_t of ~50% is achieved at St $\approx$ 0.4 for all L_n values, which corresponds to a d_p of ~1.1 µm in these simulations. Note that this is likely a lower-bound estimate of η_t in an AFL, as particles are injected uniformly across the nozzle inlet in these simulations. In an actual AFL, particles will likely be focused into a small beam to some extent by upstream lenses before reaching the nozzle. Based on these results from Figure 7b, it can be concluded that L_n has an insignificant effect on transmission efficiency. Therefore, an L_n of 0.254 mm is deemed to be the optimal length.

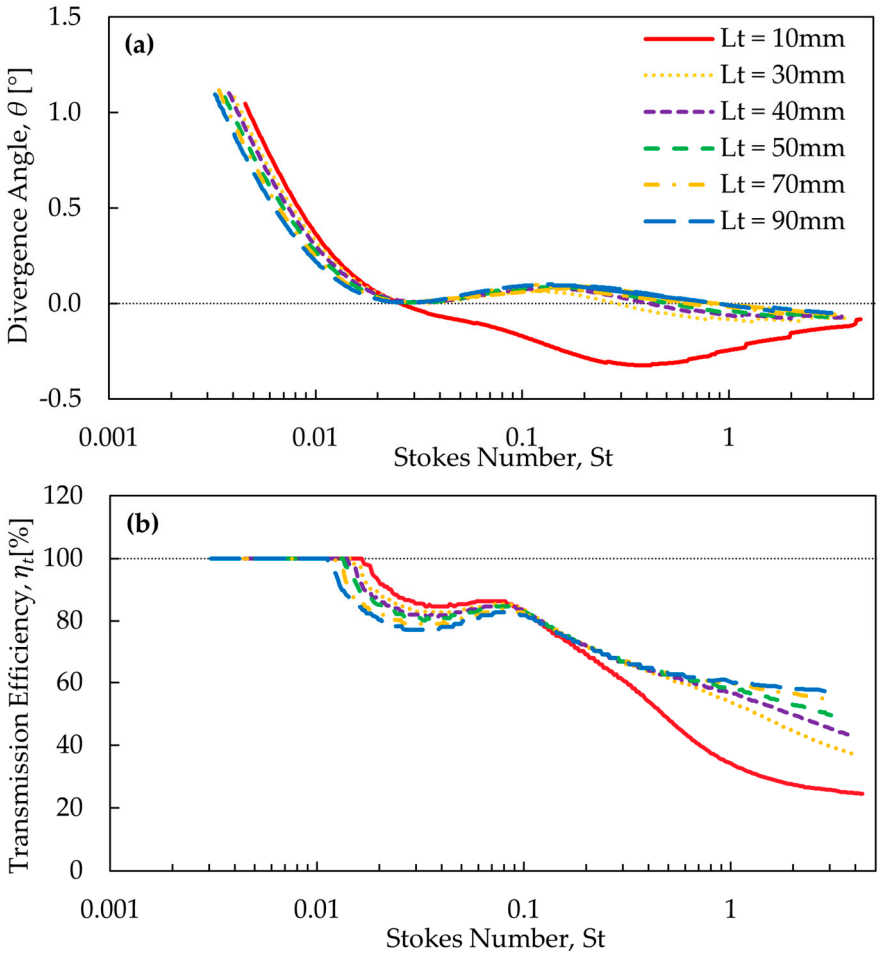

Figure 8. Results from the nozzle simulations of (**a**) θ and (**b**) η_t for various values of L_t as a function of St.

3.2.2. Step Length

Figure 8a,b show θ and η_t, respectively, as a function of St for various values of L_t with fixed R_t = 0.6 and L_n = 0.254 mm. For clarity, the results for L_t = 20, 60, and 80 mm are omitted.

Similar to the L_n results, θ for small particles with St < 0.02 decreases with St to reach a zero-divergence, regardless of the L_t value. This result indicates that neither the nozzle thickness nor the step length has a strong effect on the small particles' behavior. Past St $\approx$ 0.02, the behavior of the divergence angle is different for L_t = 10 mm compared to the other values. The divergence angle for L_t = 10 mm remains negative. However, for $L_t \geq$ 20 mm it swings between positive and negative values and remains close to a zero-divergence. At these L_t values, the divergence angle crosses the θ = 0 line twice, at St $\approx$ 0.02 and St $\approx$ 0.3–0.9, depending on L_t.

The different behavior observed for L_t = 10 mm at St > 0.02 is due to the short step length, which does not give particles sufficient distance to reach a steady horizontal trajectory within the step region compared to longer step lengths. From Figure 8a, it can be concluded that small particle divergence can be achieved with longer step lengths. However, beyond 30 mm, there is a negligible effect of L_t on particle divergence.

Figure 8b shows that particles with small St $\lesssim$ 0.01–0.015 maintain a 100% transmission efficiency for all L_t values. As St increases, a similar behavior is observed as for the L_n results, where the transmission efficiency drops below 100% at St values greater than 0.01, increases slightly, and then continuously decreases afterward. However, the value

at which St drops and the final η_t at the high St are different depending on L_t. L_t= 10 mm has the most noticeable difference from all other values. The 50% transmission efficiency is achieved at different St values. As L_t increases, the St value corresponding to a 50% transmission efficiency increases, with L_t > 60 mm maintaining a value above 50%.

Based on Figure 8, the shortest step length that can achieve, on average, the best convergence with an acceptable transmission efficiency over a wide range of St is 40 mm. Thus, this value is deemed optimal.

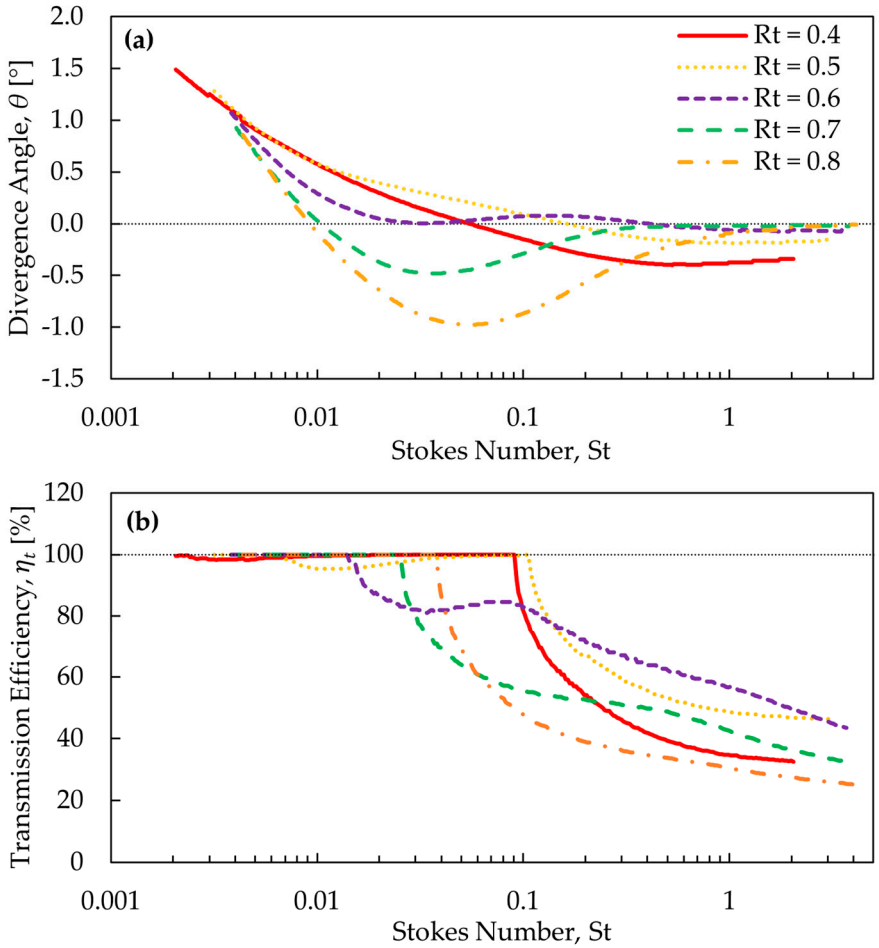

Figure 9. Results from the nozzle simulations of (**a**) θ and (**b**) η_t for various values of R_t as a function of St.

3.2.3. Step Radius

Figure 9a,b show θ and η_t, respectively, as a function of St for various values of R_t at the optimal L_n and L_t values. In these figures, St is calculated relative to d_s for consistency with previous figures. However, the particle and flow behavior inside the step will depend on the St calculated relative to the step diameter.

Figure 9a shows that the divergence angles for R_t = 0.4 and 0.5 exhibit a different behavior from larger-radius ratios. For R_t = 0.4 and 0.5, the divergence angle steadily decreases with the increase in St and then slightly increases at high St values. However, steps with $R_t \geq 0.6$ exhibit a relatively similar oscillatory behavior. R_t = 0.6 maintains a close-to-zero divergence angle for the widest range of St, while the angles for R_t = 0.7 and 0.8 significantly drop below zero and remain negative for a wide range of St. This suggests that large step radii achieve poor focusing of medium-sized particles. Large particles (St $\gtrsim$ 1) are well focused when $R_t \geq 0.6$. Based on Figure 9a, it can be concluded that an R_t value of 0.6 can maintain the best divergence angle for the widest range of St.

Figure 9b shows that, unlike L_n and L_t, η_t highly depends on the R_t value. A distinctive pattern can be noticed for small radii (R_t = 0.4 and 0.5), where the transmission efficiency initially drops below 100%, then rebounds to unity, and then drops once more at a higher St. A similar but less pronounced pattern is observed for R_t = 0.6; however, the rebound is incomplete. For larger R_t, this pattern is even less noticeable or nonexistent. Transmission efficiency in these cases drops below 100% and steadily decreases. This figure also shows that the first drop occurs at different St. However, when St is calculated based on the step diameter, the first drop below 100% occurs at the same St = 0.1 for all R_t values (see Figure S7).

The drop pattern can be explained by near-wall interaction at the step inlet. Figure 10 shows particle trajectories for the case R_t = 0.6 for two d_p values of 100 nm (St = 0.034, blue) and 200 nm (St = 0.084, red). Only 20 particles for each size are plotted for visual clarity. From the left detailed region in Figure 10, after the step restriction, the 200 nm particles with initial injection locations close to the spacer wall are focused closer to the axis due to their higher inertia compared to the 100 nm particles injected at the same location. This causes the 100 nm particles to impact on the upstream vertical surface of the exit nozzle at a higher rate than the 200 nm particles, as shown in the right detailed region of Figure 10. This behavior, noticed for step radii $R_t \leq 0.6$, nearly disappears for larger R_t, due to the smaller difference in flow velocity between the spacer and the step regions.

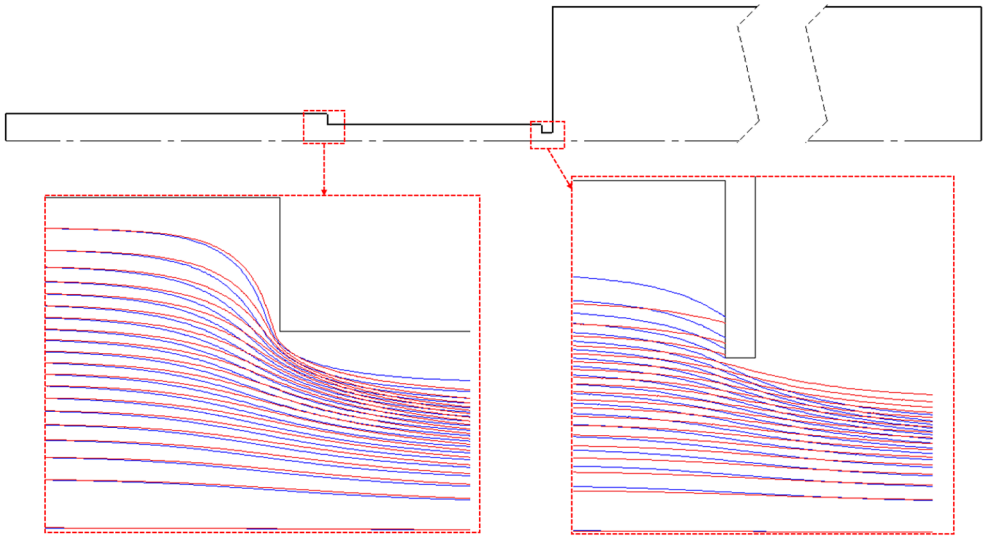

Figure 10. Trajectories of particles with two d_p values of 100 nm (blue) and 200 nm (red) at the step and nozzle inlets for the case R_t = 0.6.

From Figure 9, it can be concluded that an R_t value of 0.6 can maintain the smallest divergence angle, as well as a transmission efficiency above 50% over the widest St range. Therefore, this ratio is deemed optimal. Similar to what was initially hypothesized, an initial short capillary geometry for a step, followed by a thin plate orifice for the final nozzle outlet, results in the optimal focusing effect for particles over a wide size range.

4. Discussion and Conclusions

This paper presents the first systematic evaluation of the focusing performance of aerodynamic lenses across a wide range of α, including converging, straight-edge, and diverging orifices. It was found that the impact of α on focusing performance was not significant for near-axis particles. However, convergent lenses may better focus large particles that are near the spacer walls. For the simplicity of lens fabrication and assembly, it appears that a straight-edge orifice is the best choice.

This study further optimized the step exit nozzle geometry to focus a wide size range of particles by varying key dimensions: nozzle thickness (L_n), step length (L_t), and ratio of step radius to the spacer radius (R_t). Based on the particle divergence angle and particle transmission efficiency, an optimal geometry combination consisting of an L_n = 0.254 mm, L_t = 40 mm, and R_t = 0.6 yielded the best results over a particle size range of 10 nm–10 µm. This optimization is particularly important for efficiently delivering large particles to the vacuum chamber with low divergence angles and high transmission efficiencies, as these particles are often defocused in the final lens stages [11].

One limitation of the nozzle optimization is that it started with a d_s of 10 mm and a nozzle diameter of 3 mm. While R_t values were nondimensionalized, a fully nondimensionalized treatment of all parameters would provide a more general optimization framework. The results, however, suggest that the effect of L_n and L_t is not significant, especially on transmission efficiency. Only R_t strongly influences both the divergence angle and transmission efficiency. Thus, only nondimensionalizing R_t is justified. Liu et al. [10] studied a similar nozzle and found an optimal R_t of 0.6, although they did not optimize L_n or L_t.

Additionally, the optimization procedure subsequently varied parameters, first optimizing L_n with fixed L_t and R_t, then L_t with fixed L_n and R_t, and finally R_t. This stepwise approach may overlook the global optimum, and alternative methods such as response surface methodology or parameter interaction analysis could provide a more robust optimization strategy. Future studies should experimentally verify whether this geometry represents a truly optimal solution.

Supplementary Materials: The following supporting information can be downloaded at: https://www.mdpi.com/article/10.3390/atmos16091049/s1. S1 Flow Equations, S2 Mesh Sensitivity, and S3 Supplementary Figures. Table S1. Boundary conditions for single-lens simulations. Table S2. Grid refinement for the divergent lens model. Table S3. Grid convergence study for the convergent/divergent lens model. Table S4. Grid refinement for the nozzle model. Table S5. Grid convergence study for the nozzle model. Figure S1. Divergent lens model showing Re converging with increasing mesh quality to the Richardson extrapolation (h = 0). Figure S2. Alternate nozzle mesh study model. Figure S3. Nozzle model showing Re converging with increasing mesh quality to the Richardson extrapolation (h = 0). Figure S4. St_o as a function of α for three Ma values (0.03, 0.1, and 0.3) for near-wall particles (Δ = 0.1) at a Re of 100. Figure S5. St_o as a function of α for three Ma values (0.03, 0.1, and 0.3) for near-wall particles (Δ = 0.9) at a Re of 50. Figure S6. St_o as a function of α for three Ma values (0.03, 0.1, and 0.3) for near-wall particles (Δ = 0.9) at a Re of 100. Figure S7. Results from the nozzle simulations of η_t for various values of R_t as a function of St based on the step diameter.

Author Contributions: Conceptualization, M.H.-N. and X.W.; methodology, M.H.-N., X.W. and A.V.; software, A.V. and H.G.; formal analysis, A.V. and H.G.; investigation, A.V. and H.G.; resources, M.H.-N. and X.W.; data curation, A.V., H.G. and M.H.-N.; writing—original draft preparation, A.V.; writing—review and editing, M.H.-N. and X.W.; visualization, A.V. and H.G.; supervision, M.H.-N.; project administration, X.W.; funding acquisition, X.W. and M.H.-N. All authors have read and agreed to the published version of the manuscript.

Funding: This research received funding from the U.S. Department of Energy EPSCoR program under award number #DE-SC0021214.

Data Availability Statement: The original contributions presented in this study are included in the article. Further inquiries can be directed to the corresponding author.

Conflicts of Interest: Author Harrison Griffin was employed by Raytheon. The remaining authors declare that the research was conducted in the absence of any commercial or financial relationships that could be construed as a potential conflict of interest.

References

1. Vaden, T.D.; Imre, D.; Beránek, J.; Zelenyuk, A. Extending the Capabilities of Single Particle Mass Spectrometry: I. Measurements of Aerosol Number Concentration, Size Distribution, and Asphericity. *Aerosol Sci. Technol.* **2011**, *45*, 113–124. [CrossRef]
2. Su, Y.; Sipin, M.F.; Furutani, H.; Prather, K.A. Development and Characterization of an Aerosol Time-of-Flight Mass Spectrometer with Increased Detection Efficiency. *Anal. Chem.* **2004**, *76*, 712–719. [CrossRef] [PubMed]
3. Murphy, D.M. The design of single particle laser mass spectrometers. *Mass Spectrom. Rev.* **2007**, *26*, 150–165. [CrossRef]
4. Zelenyuk, A.; Imre, D.; Wilson, J.; Zhang, Z.; Wang, J.; Mueller, K. Airborne Single Particle Mass Spectrometers (SPLAT II & miniSPLAT) and New Software for Data Visualization and Analysis in a Geo-Spatial Context. *J. Am. Soc. Mass. Spectrom.* **2015**, *26*, 257–270. [CrossRef]
5. Israel, G.W.; Friedlander, S.K. High-Speed Beams of Small Particles. *J. Colloid Interface Sci.* **1967**, *24*, 330–337. [CrossRef]
6. Dahneke, B.E.; Flachsbart, H. An Aerosol Beam Spectrometer. *J. Aerosol Sci.* **1972**, *3*, 345–349. [CrossRef]
7. Mallina, R.V.; Wexler, A.S.; Johnston, M.V. High-Speed Particle Beam Generation: Simple Focusing Mechanisms. *J. Aerosol Sci.* **1999**, *30*, 719–738. [CrossRef]
8. Mallina, R.V.; Wexler, A.S.; Rhoads, K.P.; Johnston, M.V. High Speed Particle Beam Generation: A Dynamic Focusing Mechanism for Selecting Ultrafine Particles. *Aerosol Sci. Technol.* **2000**, *33*, 87–104. [CrossRef]
9. Liu, P.; Ziemann, P.J.; Kittelson, D.B.; McMurry, P.H. Generating Particle Beams of Controlled Dimensions and Divergence: I. Theory of Particle Motion in Aerodynamic Lenses and Nozzle Expansions. *Aerosol Sci. Technol.* **1995**, *22*, 293–313. [CrossRef]
10. Liu, P.; Ziemann, P.J.; Kittelson, D.B.; McMurry, P.H. Generating Particle Beams of Controlled Dimensions and Divergence: II. Experimental Evaluation of Particle Motion in Aerodynamic Lenses and Nozzle Expansions. *Aerosol Sci. Technol.* **1995**, *22*, 314–324. [CrossRef]
11. Wang, X.L.; McMurry, P.H. A Design Tool for Aerodynamic Lens Systems. *Aerosol Sci. Technol.* **2006**, *40*, 320–334. [CrossRef]
12. Peck, J.; Gonzalez, L.A.; Williams, L.R.; Xu, W.; Croteau, P.L.; Timko, M.T.; Jayne, J.T.; Worsnop, D.R.; Miake-Lye, R.C.; Smith, K.A. Development of an aerosol mass spectrometer lens system for PM2.5. *Aerosol Sci. Technol.* **2016**, *50*, 781–789. [CrossRef]
13. Cahill, J.F.; Darlington, T.K.; Wang, X.L.; Mayer, J.; Spencer, M.T.; Holecek, J.C.; Reed, B.E.; Prather, K.A. Development of a High-Pressure Aerodynamic Lens for Focusing Large Particles (4–10 μm) into the Aerosol Time-of-Flight Mass Spectrometer. *Aerosol Sci. Technol.* **2014**, *48*, 948–956. [CrossRef]
14. Huang, J.; Li, L.; Li, X.; Huang, Z.; Cheng, Z. Design of a wide-particle-size-range aerodynamic injection system with a new pre-focus structure. *Atmos. Meas. Tech.* **2025**, *18*, 2739–2749. [CrossRef]
15. Fernández de la Mora, J.; Riesco-Chueca, P. Aerodynamic Focusing of Particles in a Carrier Gas. *J. Fluid Mech.* **1988**, *195*, 1–21. [CrossRef]
16. Fernández de la Mora, J.; Rosell-Llompart, J.; Riesco-Chueca, P. Aerodynamic Focusing of Particles and Molecules in Seeded Supersonic Jets. In *Rarefied Gas Dynamics: Physical Phenomena, Progress in Astronautics & Aeronautics*; Muntz, E.P., Weaver, D.P., Campbell, D.H., Eds.; AIAA: Washington, DC, USA, 1989; Volume 117, pp. 247–277.
17. Middha, P.; Wexler, A.S. Particle Focusing Characteristics of Sonic Jets. *Aerosol Sci. Technol.* **2003**, *37*, 907–915. [CrossRef]
18. Wang, X.L.; Kruis, F.E.; McMurry, P.H. Aerodynamic Focusing of Nanoparticles: I. Guidelines for Designing Aerodynamic Lenses for Nanoparticles. *Aerosol Sci. Technol.* **2005**, *39*, 611–623. [CrossRef]
19. Wang, X.L.; Gidwani, A.; Girshick, S.L.; McMurry, P.H. Aerodynamic Focusing of Nanoparticles: II. Numerical Simulation of Particle Motion through Aerodynamic Lenses. *Aerosol Sci. Technol.* **2005**, *39*, 624–636. [CrossRef]
20. Zhang, L.; Shao, J.; Chen, X.; Zhang, J.; Si, Q. Design and evaluation of aerodynamic lens system for focusing sub-10 nm nanoparticles. *Appl. Phys. A* **2016**, *122*, 953. [CrossRef]
21. Zhang, X.; Smith, K.A.; Worsnop, D.R.; Jimenez, J.; Jayne, J.T.; Kolb, C.E. A Numerical Characterization of Particle Beam Collimation by an Aerodynamic Lens-Nozzle System: Part I. An Individual Lens or Nozzle. *Aerosol Sci. Technol.* **2002**, *36*, 617–631. [CrossRef]
22. Zhang, X.; Smith, K.A.; Worsnop, D.R.; Jimenez, J.L.; Jayne, J.T.; Kolb, C.E.; Morris, J.; Davidovits, P. Numerical Characterization of Particle Beam Collimation: Part II. Integrated Aerodynamic-Lens-Nozzle System. *Aerosol Sci. Technol.* **2004**, *38*, 619–638. [CrossRef]
23. Jayne, J.T.; Leard, D.C.; Zhang, X.; Davidovits, P.; Smith, K.A.; Kolb, C.E.; Worsnop, D.R. Development of an Aerosol Mass Spectrometer for Size and Composition Analysis of Submicron Particles. *Aerosol Sci. Technol.* **2000**, *33*, 49–70. [CrossRef]
24. ANSYS, Inc. *Ansys Fluent User's Guide, Release: 2022R2*; ANSYS, Inc.: Canonsburg, PA, USA, 2022.

25. Sutherland, W. The viscosity of gases and molecular force. *Philos. Mag.* **1893**, *36*, 507–531. [CrossRef]
26. Slater, J.W. Examining Spatial (Grid) Convergence; Northern Peninsula Area Regional Council (NPARC) Alliance Verification and Validation Web Site: 2021. Available online: https://www.grc.nasa.gov/www/wind/valid/tutorial/spatconv.html (accessed on 10 February 2025).

Disclaimer/Publisher's Note: The statements, opinions and data contained in all publications are solely those of the individual author(s) and contributor(s) and not of MDPI and/or the editor(s). MDPI and/or the editor(s) disclaim responsibility for any injury to people or property resulting from any ideas, methods, instructions or products referred to in the content.